

# Domain Adaptation for Robust Workload Classification using fNIRS

Boyang Lyu<sup>a,†,\*</sup>, Thao Pham<sup>b,†</sup>, Giles Blaney<sup>b</sup>, Zachary Haga<sup>c</sup>, Sergio Fantini<sup>b</sup>, Shuchin Aeron<sup>a</sup>

<sup>a</sup>Tufts University, Department of Electrical and Computer Engineering, 161 College Avenue, Medford, MA 02155

<sup>b</sup>Tufts University, Department of Biomedical Engineering, 4 Colby Street, Medford, MA 02155

<sup>c</sup>Tufts University, Department of Computer Science, 161 College Avenue, Medford, MA 02155

**Abstract.** **Significance:** We demonstrated the potential of using domain adaptation on functional Near-Infrared Spectroscopy (fNIRS) data to detect and discriminate different levels of  $n$ -back tasks that involve working memory across different experiment sessions and subjects. **Aim:** To address the domain shift in fNIRS data across sessions and subjects for task label alignment, we exploited two domain adaptation approaches - Gromov-Wasserstein (G-W) and Fused Gromov-Wasserstein (FG-W). **Approach:** We applied G-W for session-by-session alignment and FG-W for subject-by-subject alignment with Hellinger distance as underlying metric to fNIRS data acquired during different  $n$ -back task levels. We also compared with a supervised method - Convolutional Neural Network (CNN). **Results:** For session-by-session alignment, using G-W resulted in alignment accuracy of  $70 \pm 4$  % (weighted mean  $\pm$  standard error), whereas using CNN resulted in classification accuracy of  $58 \pm 5$  % across five subjects. For subject-by-subject alignment, using FG-W resulted in alignment accuracy of  $55 \pm 3$  %, whereas using CNN resulted in classification accuracy of  $45 \pm 1$  %. Where in both cases 25 % represents chance. We also showed that removal of motion artifacts from the fNIRS data plays an important role in improving alignment performance. **Conclusions:** Domain adaptation is potential for session-by-session and subject-by-subject alignment using fNIRS data.

**Keywords:** fNIRS,  $n$ -back task, machine learning, Gromov-Wasserstein (G-W), Fused Gromov-Wasserstein (FG-W), Transient Artifact Reduction Algorithm (TARA).

\*Boyang Lyu, [Boyang.Lyu@tufts.edu](mailto:Boyang.Lyu@tufts.edu)

<sup>†</sup> These authors contributed equally

## 1 Introduction

Functional near-infrared spectroscopy (fNIRS) is a noninvasive optical technique for monitoring regional tissue oxygenation based on diffusion and absorption of near-infrared light photons in human tissue. Continuous-wave fNIRS provides measurements of concentration changes in oxy-, deoxy- and total-hemoglobin species ( $\Delta[HbO_2]$ ,  $\Delta[Hb]$ , and  $\Delta[HbT]$ , respectively) in tissue with relatively good spatial resolution ( $\sim 5$  mm) and temporal resolution ( $\sim 100$  milliseconds).<sup>1</sup> Over the past three decades, fNIRS has been found in several brain imaging applications, including non-invasive imaging of cognitive involvements, brain functional activations (e.g., in motor area activation,<sup>1–3</sup> visual<sup>2,4</sup> and cognitive stimulation<sup>5,6</sup>), neuroscience,<sup>7</sup> neural rehabilitation,<sup>8</sup> and brain

computer interface (BCI).<sup>9</sup>

Memory-based workload classification using fNIRS measurements has been demonstrated to be an ideal approach for a realistic adaptive BCI to measure human workload level.<sup>10</sup> In this paper we study the problem of classification of fNIRS corresponding to different conditions of an  $n$ -back task. During an  $n$ -back task, subjects are required to continuously remember the last  $n$  ( $n \in \{1, 2, 3, \dots\}$ ) of rapidly changing items (letters or numbers). During different  $n$ -back tasks, we performed fNIRS measurements on prefrontal cortex (PFC), which has been found to be a relevant area for memory-related tasks measured by positron emission tomography (PET) and functional magnetic resonance imaging (fMRI).<sup>11,12</sup> Previous studies using fNIRS have shown that workload induced by different  $n$ -back difficulty levels results in consistent hemodynamic spatio-temporal responses in the PFC that can be classified on a single trial basis.<sup>13–15</sup> Most  $n$ -back classification studies in literature are based on supervised methods on fNIRS signals in within-session and within-subject basis (i.e., within single trial of data acquisition on a single subject).<sup>13,14,16,17</sup> While those studies showed promising results, subject- and session-depending systems are not realistic for an interface system that can adapt to different users with a wide range of physiological conditions. With the aim of use in BCI, workload classifications based on fNIRS data across experiment sessions (session-by-session alignment) and across subjects (subject-by-subject alignment) are necessary.

There are several challenges that hamper accurate workload classification using fNIRS data. We outline them below and propose methods to mitigate them.

The first challenge is **motion artifacts** in fNIRS signals. Motion artifacts in fNIRS are commonly due to the coupling changes of any source or detector from the scalp during the experiment. This causes sudden increases or decreases in measured light intensity and can affect the measured

fNIRS signals. This then leads to the misinterpretation of brain activation classification results. From a machine learning perspective, motion artifact detection and correction are crucial steps. They remove any misleading correlation from the subject behavior (twitching, head movement, etc.) to what the classification model learns from fNIRS data. For example, a classification model may be able to recognize when a subject presses a button as a requirement during the experiment by detecting spikes in the measured signals due to the subject’s head movement, instead of detecting real hemodynamic responses from the brain signals. A number of approaches, inspired by statistical signal processing methods such as adaptive filtering, independent component analysis (ICA), and time-frequency analysis, have been proposed to remove or correct for motion artifacts in fNIRS signals.<sup>18–28</sup> However, most of these techniques either depend on the use of auxiliary reference signals (e.g., accelerometry, etc) or extra optical channels, or require certain assumptions on the characteristics of motion artifacts and cleaned fNIRS signals. In this paper we used an off-the-shelf method based on sparse optimization for automatic detection and removal of spikes and steps anomalies, namely transient artifact reduction algorithm (TARA).<sup>29</sup> In the referenced study, TARA was shown to accurately preserve more hemodynamic responses in the corrected fNIRS signals than a wavelet-based approach. In this paper we will apply the method TARA in the hope to improve classification accuracy of  $n$ -back tasks.

The second challenge, which is the main focus of this paper, is to deal with **session-by-session** and **subject-by-subject** variations in classification of  $n$ -back tasks. These problems are related to what is referred to as domain adaptation in machine learning.<sup>30–32</sup> More specifically, data from different sessions or different subjects are referred to as belonging to different domains, and the changes in data distributions across different domains (the session or subject that the data belongs to) are considered as a domain shift.<sup>33</sup> Due to this phenomenon, the knowledge we learned from

one domain can't be applied directly to another one. We systematically exploited recent advances in the theory and methods of optimal transport (OT)<sup>34</sup> and metric measure space alignment<sup>35,36</sup> to address the variability in data acquired during each  $n$ -back condition across different experimental sessions and different subjects. In particular, data with known labeled  $n$ -back condition from one session or one subject could be used to align it to the unlabeled data from different session within the same subject or from different subject. Though OT has been applied for domain adaptation with potential performance,<sup>37–39</sup> it has some limitations when two sets of data used for alignment do not share the same metric space, in which case a meaningful notion on distance between two spaces does not exist. For example, for session-by-session alignment, some channels of the measured fNIRS data may need to be removed from one of the two sessions due to a poor signal-to-noise (SNR) ratio. This will cause two sessions' data being embedded in different dimensions in the two domains. A naïve solution is to remove the corresponding channels from the other session to guarantee that the two sessions have the same dimension. However, this has a disadvantage of causing loss of information. In this paper, we proposed that using Gromov-Wasserstein (G-W)<sup>36,40</sup> and fused Gromov-Wasserstein (FG-W) barycenter<sup>41</sup> alleviated this problem and provided algorithms to align across domains for fNIRS  $n$ -back task classification.

The main contributions contained within this paper to the classification of different  $n$ -back task conditions include: (1) applying G-W to align fNIRS data during each  $n$ -back task condition across different experimental sessions for every single subject (session-by-session alignment); (2) applying FG-W barycenter to align fNIRS data during each  $n$ -back condition between different subjects (subject-by-subject alignment); and (3) demonstrating that our method requires less amount of labeled data than supervised methods, such as convolutional neural network (CNN).

The remainder of the paper is organized as follows: **Section 2** describes the experiment we

conducted to acquire fNIRS data during  $n$ -back tasks; **Section 3** presents the background of G-W and FG-W barycenter as well as the algorithm for  $n$ -back task alignment; **Section 4** presents results of session-by-session and subject-by-subject alignment; and **Section 5** is the discussion and conclusion of our study.

## **2 Experiment**

### *2.1 Subjects and Experiment Design*

Five healthy human subjects (one female, age range: 23-54 years) participated in this study. All subjects have normal or corrected to normal vision. The Tufts University Institutional Review Board approved the experimental protocol, and the subjects provided written informed consent prior to the experiment.

During the  $n$ -back task, subjects were instructed to watch a series of rapidly flashing random one-digit numbers (from 0-9) shown on a computer screen. The screen was placed ~50 cm in front of the subject. Subjects must continuously remember the last  $n$  numbers and were asked to press the space bar if the currently displayed number (target) matched the preceding  $n$ -th number. With increasing  $n$ , the task difficulty is expected to increase, as the subjects must remember an increasing number of preceding digits and continuously shift the remembered sequence. The experiment was designed such that the targets appeared with 25-35 % chance (i.e., 65-75 % non-targets) in each task (chosen randomly). We measured the task performance by counting the number of missed targets (when the subject did not press the space bar for a target), and the number of wrong reactions (when the subject incorrectly identified a non-target stimulus as a target).

Each subject performed a total of four separate experiment sessions in two days: two sessions per day, one in the morning shift (9-12 a.m.) and one in the afternoon shift (1-4 p.m.). Each

experiment session consisted of four blocks of 0-, 1-, 2-, and 3-back tasks ( $n = 0, 1, 2, \text{ and } 3$ ). The order of the tasks was randomized among sessions, but the randomization order was kept the same among subjects (i.e. only four random sequences were used and each subject was shown each of the four after all of their sessions). In the 0-back task, the subject pressed the space bar whenever numeral “0” (target) appeared on the screen. A session started with 155 sec of initial baseline with a countdown timer displayed on the screen. At the beginning of a task, an instruction was shown to inform the subject that the upcoming task was 0-, 1-, 2- or 3-back. A task consisted of 100 displayed digits each lasting 2 sec, during which stimulus was displayed for 1.5 sec and followed by a resting time of 0.5 sec where a black screen was shown. Therefore, each task was a total of 200 sec in length. Subsequently, the subject entered 30 sec of baseline (rest) after finishing the task while the performance accuracy of the preceding task was displayed on the screen. This process was repeated for the four values of  $n$ . At the end of the fourth task, the subject rested for a 155 sec baseline after which the experiment was completed. Figure 1a shows the experiment protocol. The entire experiment had a recording time of 20 min (four 200-sec tasks, two 155-sec baselines, and three 30-sec rests in the middle).

## *2.2 fNIRS Data Acquisition*

During the entire experiment session, optical data were collected continuously with a continuous-wave fNIRS device (NIRScout, NIRx Medical Technology, Berlin, Germany). Eight light emitting diode (LED) source pairs (at two wavelengths of 760 and 850 nm) and seven detector fiber bundles connected to photodiode (PD) detectors were arranged on a conformable fabric headset. The fNIRS headset can be quickly fixed to the forehead to enable high quality measurements of the prefrontal cortex (PFC) within the range of several minutes. A total of 20 source-detector channels at 3 cm

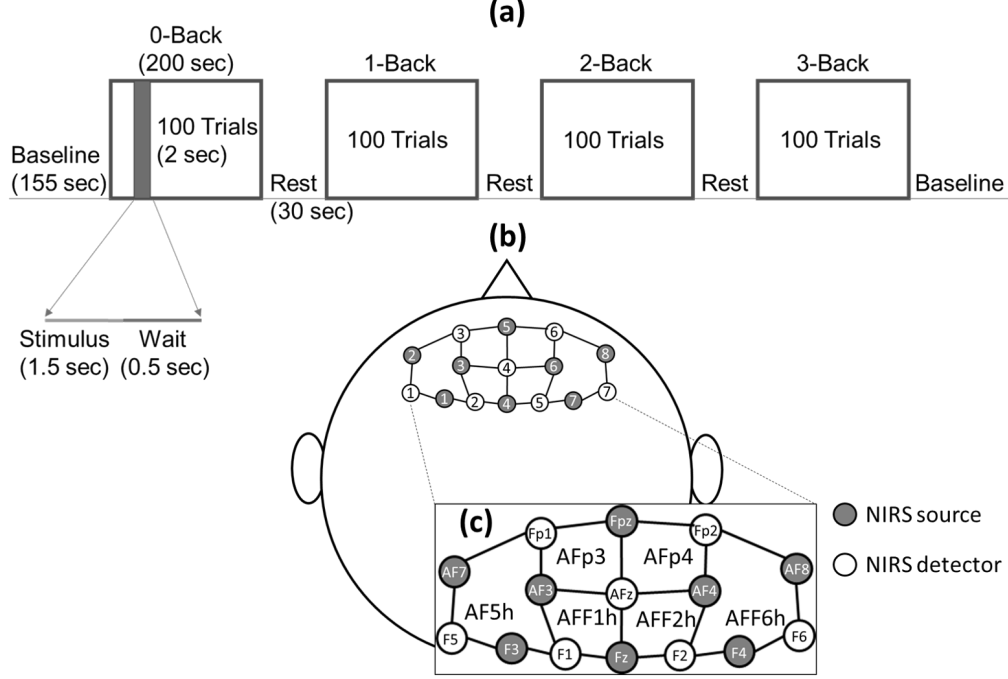


Fig 1: (a) Experimental design for  $n$ -back task. (b) fNIRS headset with eight sources and seven detectors to give a total of 20 channels at source-detector distance of 3 cm. (c) A zoomed-in view of the schematic in (b) showing the 10-10 and 10-5 system positions covered by the sources and detectors.

source-detector distances were collected. The channels covered the PFC at 15 positions according to the 10-10 international system (Fp1, Fpz, Fp2, AF7, AF3, AFz, AF4, AF8, F5, F3, F1, Fz, F2, F4 and F6) and 6 positions according to the 10-5 international system (AFp3, AFp4, AF5h, AFF1h, AFF2h, and AFF6h).<sup>42</sup> A schematic diagram of the arrangement is shown in Fig. 1b, c.

Light intensities were collected at a sampling rate of 7.81 Hz. Linear detrending was applied to the collected changes in light intensity with respect to baseline to remove slow temporal drifts. Then the detrended normalized intensities were converted into  $\Delta[HbO_2]$  and  $\Delta[Hb]$  by using the modified Beer-Lambert law.<sup>43</sup> We assumed the wavelength-dependent differential pathlength factors (DPFs), which account for the increase in photon pathlength due to multiple scattering, equal to 9.1 and 8.0 for 760 and 850 nm, respectively.<sup>44</sup>

Measured fNIRS data was then plotted and checked manually to remove channels with poor

SNR. To further exclude the motion artifacts, we used the TARA algorithm,<sup>29</sup> in which measured time series data are treated as a linear combination of a low-pass signal, motion artifacts and white noise. The algorithm focuses on two types of motion artifacts, namely transient pulses (spike-like signals) and step discontinuities, and assumes both of them appear infrequently. A sparse optimization problem is then formulated to jointly estimate two types of motion artifacts. We refer the reader to<sup>29</sup> for details. We used the code provided by the authors<sup>1</sup> and adapted the parameters for our fNIRS data. Once the motion artifacts are detected, they can be removed from the original signal to obtain the cleaned data.

### 3 Domain adaptation for fNIRS

After the removal of the channels with poor SNR and motion artifacts, a small time duration  $w$  is chosen as the window size to divide the remaining  $n$ -back data ( $\Delta[HbO_2]$  and  $\Delta[Hb]$ ) into  $N$  non-overlap small segments. Here we use  $w = 60$  samples (~8 sec). In order to concretely describe the proposed method, next we will set some notation that is used throughout the paper.

**Notation:** We will use lower-case boldface letters  $\mathbf{x}$  to denote vectors and upper case bold-face letters  $\mathbf{X}$  to denote matrices. Unless otherwise stated, un-bolded lower case letters denote scalars.  $\{(\mathbf{X}_{m,i}^s, y_{m,i}^s)\}_{i=1}^N$  stands for the collection of segmented data set of subject  $s$  in its  $m_{th}$  session, where  $N$  is the number of segments, integer  $s \in [1, 5]$ , and integer  $m \in [1, 4]$ . The  $i$ -th segment is denoted as  $\mathbf{X}_{m,i}^s \in \mathbb{R}^{d \times w}$ , where  $d$  is the number of channels and  $w$  is the window length.  $y_{m,i}^s \in [0, 3]$  is the corresponding  $n$ -back task label for subject  $s$  in session  $m$ ,  $\mathbf{y}_m^s = \mathbf{vec}(y_m^s)$  is a  $N$  dimensional vector of the label. The remaining notation will be introduced as needed.

---

<sup>1</sup><http://eeweb.poly.edu/iselesni/TARA/index.html>



### 3.1 Session-by-session Alignment

#### 3.1.1 Optimal Transport Theory and Gromov-Wasserstein Matching

Consider two discrete sets of points  $\{\mathbf{x}_i\}_{i=1\dots n}, \mathbf{x}_i \in \mathbb{R}^d$  in a metric space  $\mathcal{X}$  with a metric  $d_{\mathcal{X}}$ , and  $\{\mathbf{y}_j\}_{j=1\dots m}, \mathbf{y}_j \in \mathbb{R}^d$  in another metric space  $\mathcal{Y}$  with the metric  $d_{\mathcal{Y}}$ . The main idea behind aligning two sets of points is by viewing them as two empirical distributions,

$$\mathbf{a} = \sum_{i=1}^n \mathbf{a}_i \delta_{\mathbf{x}_i}, \mathbf{b} = \sum_{j=1}^m \mathbf{b}_j \delta_{\mathbf{y}_j} \quad (1)$$

where  $\delta_{\mathbf{x}_i}$  and  $\delta_{\mathbf{y}_j}$  are Dirac functions at the position of  $\mathbf{x}_i$  and  $\mathbf{y}_j$ ,  $\mathbf{a}_i$  and  $\mathbf{b}_j$  are the corresponding probabilities. Without further information,  $\mathbf{a}_i$  and  $\mathbf{b}_j$  will be set as  $\frac{1}{n}$  and  $\frac{1}{m}$  respectively. The Optimal transport (OT) problem is proposed to find a plan  $\mathbf{T} \in \mathbb{R}^{n \times m}$  that is the solution to

$$\arg \min_{\mathbf{T} \in U(\mathbf{a}, \mathbf{b})} \langle \mathbf{C}, \mathbf{T} \rangle \quad (2)$$

where  $\langle \mathbf{C}, \mathbf{T} \rangle = \sum_{i,j} \mathbf{C}_{i,j} \mathbf{T}_{i,j}$ ,  $U(\mathbf{a}, \mathbf{b}) = \{\mathbf{T} \in \mathbb{R}_+^{n \times m} : \sum_{j=1}^m \mathbf{T}_{i,j} = \mathbf{a}_i, \sum_{i=1}^n \mathbf{T}_{i,j} = \mathbf{b}_j\}$ ,  $\mathbf{C} \in \mathbb{R}^{n \times m}$  with the  $i, j$ -th element  $\mathbf{C}_{i,j}$  being the cost of associating (moving) the point  $\mathbf{x}_i$  to the point  $\mathbf{y}_j$ . This is also known as the Kantorovich's relaxation<sup>45</sup> for the original Monge problem.<sup>46</sup> To reduce the computational cost of solving the linear program Eq. (2), an entropic regularization term is usually added to Eq. (2), leading to:

$$\min_{\mathbf{T} \in U(\mathbf{a}, \mathbf{b})} \langle \mathbf{C}, \mathbf{T} \rangle - \lambda H(\mathbf{T}) \quad (3)$$

where  $H(\mathbf{T}) = -\sum_{i,j} \mathbf{T}_{i,j}(\log \mathbf{T}_{i,j} - 1)$ . This entropic OT problem<sup>47</sup> can be solved efficiently using the Sinkhorn Algorithm<sup>48</sup> or its variations such as the Greenkhorn algorithm,<sup>49</sup> both of which can achieve a near-linear time complexity.<sup>50</sup> This approach has been used in domain adaptation<sup>37-39</sup> for transfer of data in different domains.

Though widely used for domain adaptation, classic OT lacks the ability of mapping two different metric spaces. When the points have different dimensions, i.e.  $\mathbf{x}_i \in \mathbb{R}^{d_1}$  and  $\mathbf{y}_j \in \mathbb{R}^{d_2}$ , where  $d_1 \neq d_2$ , a distance between  $\mathbf{x}_i$  and  $\mathbf{y}_j$  may not be meaningfully defined. Thus, instead of seeking a distance matrix between elements in different domains, Gromov-Wasserstein (G-W) method compares the distance between the pair-wise dissimilarity in each domain. It poses a weaker assumption that if  $\mathbf{x}_i$  should be aligned to  $\mathbf{y}_j$  and  $\mathbf{x}_{i'}$  should be aligned to  $\mathbf{y}_{j'}$ , then for two distance matrices  $\mathbf{C}^{\mathcal{X}} \in \mathbb{R}^{n \times n}$  and  $\mathbf{C}^{\mathcal{Y}} \in \mathbb{R}^{m \times m}$  in space  $\mathcal{X}$  and  $\mathcal{Y}$ ,  $\mathbf{C}_{i,i'}^{\mathcal{X}}$  and  $\mathbf{C}_{j,j'}^{\mathcal{Y}}$  should share the similarity.<sup>35</sup> Formally, the G-W distance is defined as

$$GW((\mathbf{a}, \mathbf{C}^{\mathcal{X}}), (\mathbf{b}, \mathbf{C}^{\mathcal{Y}})) = \min_{\mathbf{T} \in U(\mathbf{a}, \mathbf{b})} \sum_{i,i',j,j'} L(\mathbf{C}_{i,i'}^{\mathcal{X}}, \mathbf{C}_{j,j'}^{\mathcal{Y}}) \mathbf{T}_{i,j} \mathbf{T}_{i',j'} \quad (4)$$

where  $L$  is a cost function, which typically can be chosen as a quadratic function or Kullback-Leibler divergence. Eq. (4) is a non-convex problem related to Quadratic Assignment Problem (QAP),<sup>36</sup> which is NP-hard. A regularized version of Gromov-Wasserstein problem is proposed in,<sup>35</sup> written as

$$GW_{\lambda}((\mathbf{a}, \mathbf{C}^{\mathcal{X}}), (\mathbf{b}, \mathbf{C}^{\mathcal{Y}})) = \min_{\mathbf{T} \in U(\mathbf{a}, \mathbf{b})} \sum_{i,i',j,j'} L(\mathbf{C}_{i,i'}^{\mathcal{X}}, \mathbf{C}_{j,j'}^{\mathcal{Y}}) \mathbf{T}_{i,j} \mathbf{T}_{i',j'} - \lambda H(\mathbf{T}) \quad (5)$$

Problem in Eq. (5) can be solved by projected gradient descent algorithm wherein each iteration

solution is found by running Sinkhorn Algorithm.<sup>40</sup>

### 3.1.2 Metric for G-W Alignment for fNIRS data

For EEG and fNIRS processing, mean and covariance of the time segments have been considered as useful features,<sup>51,52</sup> here we use these features to compute the inner metric matrix of each session.

Specifically, for data  $\{\mathbf{X}_{m,i}^s\}_{i=1}^N$  from  $m_{th}$  session of subject  $s$ , we compute its covariance matrices  $\{\mathbf{P}_{m,i}^s\}_{i=1}^N$  and mean vectors  $\{\mathbf{h}_{m,i}^s\}_{i=1}^N$ , where  $\mathbf{P}_{m,i}^s \in \mathbb{R}^{d \times d}$ ,  $\mathbf{h}_{m,i}^s \in \mathbb{R}^d$ . The distance matrix  $\mathbf{C}_m^s \in \mathbb{R}^{N \times N}$  is then defined with the  $i, i'$ -th element  $(\mathbf{C}_m^s)_{ii'}$  set as

$$(\mathbf{C}_m^s)_{ii'} = (\rho_{hellinger}(\mathbf{P}_{m,i}^s, \mathbf{P}_{m,i'}^s) + \|\mathbf{h}_{m,i}^s - \mathbf{h}_{m,i'}^s\|_2)/d \quad (6)$$

where  $\rho_{hellinger}(\cdot)$  is the matrix version of Hellinger distance,<sup>53</sup> written as

$$\rho_{hellinger}(\mathbf{A}, \mathbf{B}) = (tr(\mathbf{A} + \mathbf{B}) - 2tr(\mathbf{A}^{1/2}(\mathbf{A}^{-1/2}\mathbf{B}\mathbf{A}^{-1/2})^{1/2}\mathbf{A}^{1/2}))^{1/2} \quad (7)$$

where  $\mathbf{A}$  and  $\mathbf{B}$  are Positive Definite (PD) matrices. Since the number of channels  $d$  selected for different sessions' data are not necessarily the same, we normalize by the number of channels in each session.

### 3.1.3 Domain Adaptation for Session-by-session Alignment

We assume the label is given for one session's data and aim to infer the label for all other sessions belonging to the same subject. Using the metric defined in Eq. (6), we show the pseudocode for the session-by-session alignment in Algorithm 1. Since we only consider data within the same subject, upper index for subject will be dropped in the algorithm.

---

**Algorithm 1** Alignment between session  $m$  and session  $n$ 

---

**Input:** Source data and label  $\{(\mathbf{X}_{m,i}, y_{m,i})\}_{i=1}^N$ , target data  $\{\mathbf{X}_{n,i}\}_{i=1}^N$

**Output:** Target label  $\{y_{n,i}\}_{i=1}^N$

- 1: Calculate inner distance matrices  $\mathbf{C}_m$  and  $\mathbf{C}_n$  using Eq. (6) for  $\{\mathbf{X}_{m,i}\}_{i=1}^N$  and  $\{\mathbf{X}_{n,i}\}_{i=1}^N$ .
  - 2: Solve Eq. (5) to get the transport plan  $\mathbf{T}$  between session  $m$  and session  $n$ .
  - 3: Choose the largest value of each column of  $\mathbf{T}$  as 1 and set others to be 0 to get the coupling matrix  $\mathbf{T}_{cp}$
  - 4: Get target label  $\{y_{n,i}\}_{i=1}^N$  by calculating  $\mathbf{T}_{cp}^\top \mathbf{vec}(y_m)$
- 

### 3.2 Subject-by-subject Alignment

When targeting subject-by-subject alignment, we assume data and the corresponding labels for all sessions of one subject are given and denote this subject as the source subject. Then we will use these information to predict the labels of fNIRS data for all four sessions of other subjects (target subjects). Transferring labels between different subjects is a bigger challenge since there is a larger shift in domain. Directly using the same G-W alignment as discussed above will lead to a large variance in alignment accuracy. More importantly, we will lose the advantage of knowing all the features and structural information from multiple sessions of the source subject. To address this problem, we considered a recently proposed method named Fused Gromov-Wasserstein (FG-W).<sup>41</sup> By computing a FG-W barycenter, which is the Fréchet mean of FG-W distance, we summarized all the given information into a new representation of the source subject and then follow the same routine as session-by-session alignment to achieve the label alignment.

#### 3.2.1 Fused Gromov-Wasserstein Barycenter

Fused Gromov-Wasserstein, unlike the G-W, combines both feature and structural information and shows its advantage in graph classification.<sup>41,54</sup> Consider two sets of tuples  $\{(\mathbf{x}_i, \mathbf{f}_i)\}_{i=1 \dots n}$  in space  $(\mathcal{X}, \Sigma)$  and  $\{(\mathbf{y}_j, \mathbf{g}_j)\}_{j=1 \dots m}$ , in space  $(\mathcal{Y}, \Sigma)$ , here  $\mathbf{x}_i \in \mathbb{R}^{d_1}$  and  $\mathbf{y}_j \in \mathbb{R}^{d_2}$  are the data

points,  $\mathbf{f}_i$  and  $\mathbf{g}_j$  are their corresponding features which are both in space  $\Sigma$  and share the same dimension. With a slight abuse of notation, we will use the same symbol as Eq. (1) to denote their empirical distribution,

$$\mathbf{a} = \sum_{i=1}^n \mathbf{a}_i \delta_{(\mathbf{x}_i, \mathbf{f}_i)}, \mathbf{b} = \sum_{j=1}^m \mathbf{b}_j \delta_{(\mathbf{y}_j, \mathbf{g}_j)} \quad (8)$$

The FG-W distance is then defined as

$$FGW(\mathbf{a}, \mathbf{b}) = \min_{\mathbf{T} \in U(\mathbf{a}, \mathbf{b})} \sum_{i, i', j, j'} ((1 - \alpha) \rho(\mathbf{f}_i, \mathbf{g}_j)^q + \alpha |\mathbf{C}_{i, i'}^{\mathcal{X}} - \mathbf{C}_{j, j'}^{\mathcal{Y}}|^q) \mathbf{T}_{i, j} \mathbf{T}_{i', j'} \quad (9)$$

where  $\alpha \in [0, 1]$  is a trade-off parameter,  $q \geq 1$ ,  $\rho(\mathbf{f}_i, \mathbf{g}_j)$  stands for the cost of matching feature  $\mathbf{f}_i$  to feature  $\mathbf{g}_j$  which in our case corresponds to the labels, i.e. scalar value  $n$  in the  $n$ -back task.

For multiple distribution setting, a natural extension of FG-W is its barycenter, which inherits the advantages of FG-W that leverages both structural and feature information. The FG-W barycenter can be obtained by minimizing the weighted sum of a set of FG-W distances. Let  $\{\mathbf{C}^k\}_{k=1}^K$  be a set of distance matrices, where  $\mathbf{C}^k \in \mathbb{R}^{N \times N}$ ,  $\{\mathbf{f}^k\}_{k=1}^K$ ,  $\mathbf{f}^k \in \mathbb{R}^N$  is the corresponding feature vector. Here  $K$  will correspond to the number of sessions for each subject in our case. We assume the base histograms  $\{\mathbf{a}^k\}_{k=1}^K$  and the histogram  $\mathbf{a}$  associated with the barycenter is known and fixed. By calculating the Fréchet mean of the FG-W distance, we aim to find a feature vector  $\mathbf{f}$  and a structure matrix  $\mathbf{C}$ , such that

$$\min_{\mathbf{C} \in \mathbb{R}^{N \times N}, \mathbf{f} \in \mathbb{R}^N, (\mathbf{T}^k)_k \in U(\mathbf{a}, \mathbf{a}^k)} \sum_k \sum_{i, i', j, j'} \lambda_k ((1 - \alpha) d(\mathbf{f}_i, \mathbf{f}_j^k)^q + \alpha |\mathbf{C}_{i, i'} - \mathbf{C}_{j, j'}^k|^q) \mathbf{T}_{i, j}^k \mathbf{T}_{i', j'}^k \quad (10)$$

where  $\sum_k \lambda_k = 1$  and  $q \geq 1$ . This problem can be solved by Block Coordinate Descent (BCD) algorithm described in.<sup>41</sup>

### 3.2.2 Metric for FG-W Barycenter Alignment

Unlike the metric defined in Eq. (6) for session-by-session alignment, we removed the L2 norm of the mean difference from the distance when considering the metric for subject-by-subject alignment. This is because the differences of the mean values are usually the same within the same subject but vary across different subjects. It's worth to mention that after removing the L2 norm of the mean difference, the covariance matrices themselves can be viewed as points in a Riemannian space.<sup>55</sup> Formally, for the  $m_{th}$  session of subject  $s$ , the distance matrix  $C_m^s$  is defined using its covariance matrices  $\{P_{m,i}^s\}_{i=1}^N$ ,  $P_m^s \in \mathbb{R}^{d \times d}$ , with the  $i, i'$ -th element  $(C_m^s)_{ii'}$  computed via,

$$(C_m^s)_{ii'} = ((tr(P_{m,i}^s + P_{m,i'}^s) - 2tr((P_{m,i}^s)^{1/2}((P_{m,i}^s)^{-1/2}P_{m,i'}^s(P_{m,i}^s)^{-1/2})^{1/2}(P_{m,i}^s)^{1/2}))^{1/2})/d \quad (11)$$

### 3.2.3 Domain Adaptation for Subject-by-subject Alignment

The algorithm for subject-by-subject alignment is shown in Algorithm 2, here we only take two subjects as an example but the algorithm can be easily adapted to all other subjects.

---

#### Algorithm 2 Alignment between subject $s$ and subject $t$

---

**Input:** Source data and label  $\{(X_{\{1...4\},i}^s, y_{\{1...4\},i}^s)\}_{i=1}^N$ , **target data**  $\{X_{\{1...4\},i}^t\}_{i=1}^N$

**Output:** Target label  $\{y_{\{1...4\},i}^t\}_{i=1}^N$

---

- 1: For source and target data, calculate two lists of distance matrices  $[C_1^s, C_2^s, C_3^s, C_4^s]$  and  $[C_1^t, C_2^t, C_3^t, C_4^t]$  respectively using Eq. (11).
  - 2: Solve Eq. (10) using  $[(C_1^s, \mathbf{y}_1^s), (C_2^s, \mathbf{y}_2^s), (C_3^s, \mathbf{y}_3^s), (C_4^s, \mathbf{y}_4^s)]$  to get the inner distance matrix and corresponding label vector of the barycenter for subject  $s$ , denoted as  $\{C_{bary}^s, \mathbf{y}_{bary}^s\}$ .
  - 3: Repeat Step 2 to 4 in Algorithm 1 using  $\{C_{bary}^s, \mathbf{y}_{bary}^s\}$  and  $[C_1^t, C_2^t, C_3^t, C_4^t]$  as input to get the labels  $\{y_{\{1...4\},i}^t\}_{i=1}^N$  for target data.
-

## 4 Results

### 4.1 Subject Performance

To confirm that the subjects perceived different  $n$ -back task conditions as different, we analyzed subject performance. We evaluated the number of wrong responses (when subjects incorrectly identified a stimulus number as a target and pressed the key) and the number of missed responses (when a subject failed to press the key when a target stimulus was presented) in each experimental session.

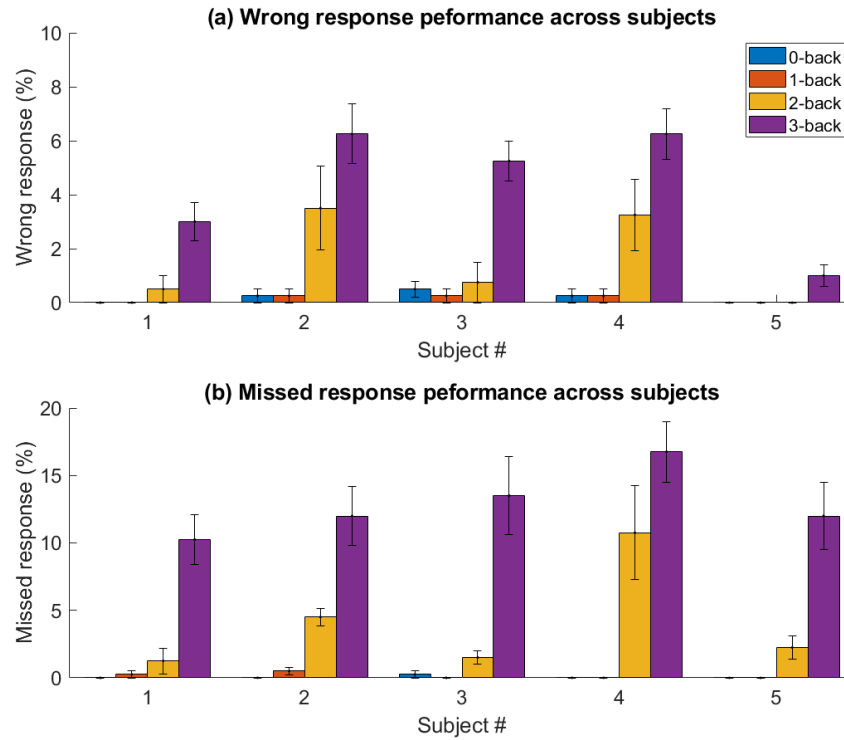


Fig 2: Summary of subject performance for the  $n$ -back task: average percentages of wrong responses (a) and missed responses (b) for  $n$ -back task conditions across subjects. Bars represent the mean, and error bars represent standard errors across four experimental sessions.

Figure 2 shows the summary of the subject performance analysis for the  $n$ -back task across five subjects with the average percentages of wrong and missed responses, respectively, across four sessions for each  $n$ -back task condition over five subjects. The difficulty level, in terms of the

amounts of wrong and missed responses, increases significantly for the 3-back task as compared to other  $n$ -back tasks in all four sessions and five subjects (non-parametric Wilcoxon signed rank test,  $p < 0.05$ ). Next, the amounts of wrong and missed responses for 2-back task in the four experiment sessions are significantly higher than for the 1- and the 0-back task ( $p < 0.05$ ). Finally, there was no significant difference in the difficulty level between the 0- and the 1-back task in terms of wrong and missed responses ( $p > 0.05$ ).

#### 4.2 Effects of Motion Artifact Removal using TARA

Figure 3 displays the effects of TARA in removing motion artifacts in fNIRS signals ( $\Delta[Hb]$ ). As shown in the figure, the original signal is contaminated by the motion artifacts including spikes and steps. After applying TARA algorithm, most of the motion artifacts have been removed. As compared to applying low-pass filter to the original signal, TARA does not bring any further distortion to the cleaned signal and is more effective at removing step artifacts. The effect of this motion artifacts removal as a pre-processing step before applying alignment algorithms is also shown in Table 1. An improvement for session-by-session alignment accuracy (by an average of  $13 \pm 3\%$  across five subjects) and subject-by-subject alignment accuracy (by an average of  $11 \pm 2\%$  across five subjects) can be seen after applying TARA on fNIRS signals. All values are reported as mean  $\pm$  standard error weighted by the standard deviations of the alignment accuracy values from five subjects.

#### 4.3 Session-by-session Alignment

A low dimensional UMAP (uniform manifold approximation and projection)<sup>56</sup> visualization of the alignment for two sessions' data is shown in Fig. 4. Note that in Fig. 4 the low dimensional



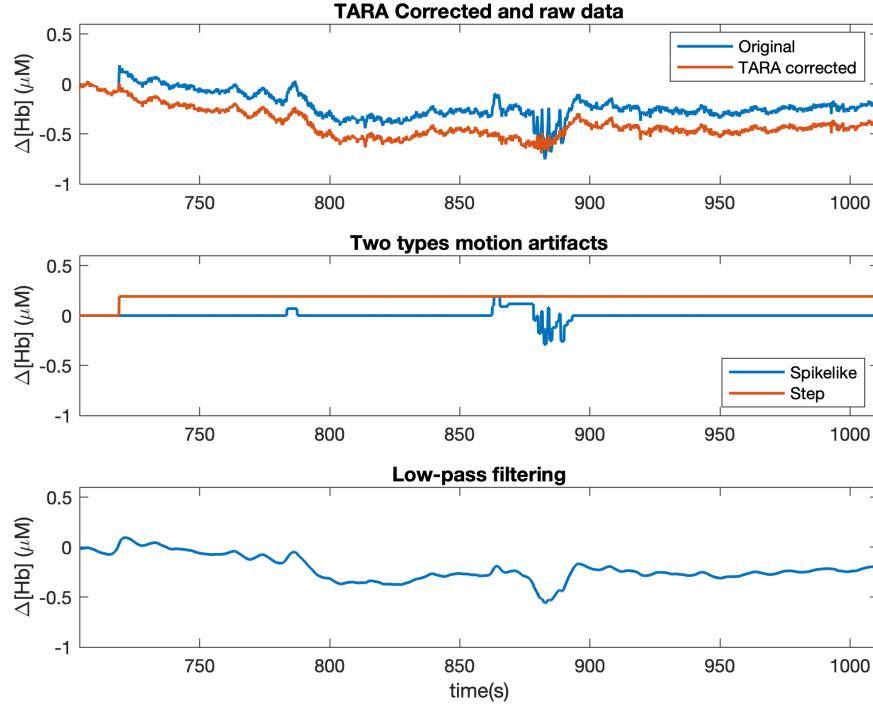


Fig 3: The top row shows the original and cleaned signal. The second row shows the detected motion artifacts, including spike- and step-like features. The cleaned signal is obtained by subtracting these motion artifact features from the original signal. The last row shows the low-pass filtered signal of the original data. Distortion in the signal arisen from the step discontinuity can still be observed from the low-pass filtered signal.

projection was generated individually from the distance matrix of each session's data. Therefore, the positions of the two groups of sessions' data are assigned randomly and their relative distances are not their true distances.

Figure 5a presents the confusion matrices of session-by-session alignment for four  $n$ -back tasks (0, 1, 2, and 3) of five subjects. Numbers reported in the confusion matrix are the average alignment accuracy of all the possible combinations of two out of all four sessions for each subject. Values in the main diagonal of each confusion matrix represent correct alignment between predicted and true label, while the other values represent the misalignment results. We also summarize the averages and standard deviations of session-by-session alignment accuracy for five subjects in Table 1. Each accuracy value reported in Table 1 for G-W corresponds to the average of the main diagonal of each

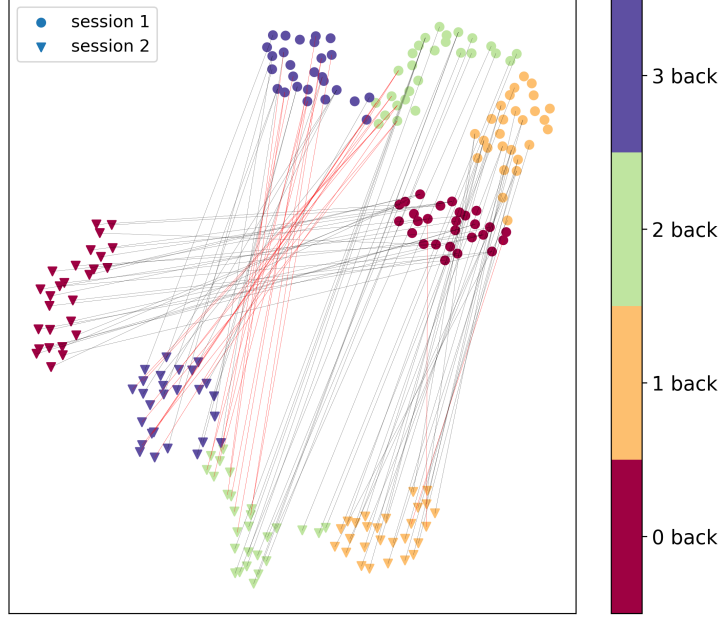


Fig 4: Visualization of the alignment from session 1 to session 2 for subject 4. Circles indicate data from session 1 and triangles indicate the data from session 2. Four different colors represent 0- to 3-back experiments. Black lines indicate correct alignment and red lines indicate misalignment.

confusion matrix.

To further demonstrate the potential of our method, we compared our method with a convolutional neural network (CNN) which was designed based on EEG-NET.<sup>57</sup> We simplified the CNN architecture to 3 convolutional layers followed by 2 dense layers (details can be found in Appendix Table 6). During the training process for CNN, the cleaned  $\Delta[HbO_2]$  and  $\Delta[Hb]$  data were first separated and stacked up. Since the removal of some noisy channels will lead to the input data in different dimensions, which will cause the mismatch between input data and the fixed model structure, we replaced the discarded channels with the average of data from the remaining channels (separately for  $\Delta[HbO_2]$  and  $\Delta[Hb]$ ). We used data from one session as input to train the model with Adam optimizer.<sup>58</sup> To guarantee the best test accuracy can be obtained, the model was trained until severe overfitting happened (300 epochs in our case). Test accuracy was recorded during the whole training process (i.e. after each training epoch) and the best result was selected among them.

Table 1: Average session-by-session and subject-by-subject alignment accuracy (%) by using G-W and FG-W, respectively, as compared with CNN. G-W and FG-W barycenter alignment methods are applied to both original data and data cleaned by TARA algorithm. For CNN, only cleaned data are used as input.

|                    |               | Subject 1   | Subject 2   | Subject 3   | Subject 4   | Subject 5   |
|--------------------|---------------|-------------|-------------|-------------|-------------|-------------|
| session-by-session | CNN cleaned   | $60 \pm 7$  | $37 \pm 11$ | $40 \pm 12$ | $58 \pm 11$ | $70 \pm 7$  |
|                    | G-W original  | $54 \pm 17$ | $58 \pm 12$ | $48 \pm 23$ | $76 \pm 13$ | $75 \pm 7$  |
|                    | G-W cleaned   | $54 \pm 8$  | $63 \pm 16$ | $62 \pm 21$ | $76 \pm 13$ | $77 \pm 5$  |
| subject-by-subject | CNN cleaned   | $43 \pm 13$ | $48 \pm 17$ | $47 \pm 15$ | $45 \pm 21$ | $42 \pm 16$ |
|                    | FG-W original | $50 \pm 12$ | $58 \pm 10$ | $49 \pm 6$  | $55 \pm 13$ | $55 \pm 10$ |
|                    | FG-W cleaned  | $55 \pm 13$ | $68 \pm 15$ | $51 \pm 4$  | $64 \pm 17$ | $67 \pm 10$ |

The training and testing processes were conducted 5 times and the average test accuracy for each subject was reported in Table 1. As shown in this table, classification accuracy from CNN is lower than the alignment accuracy from G-W by an average of  $7 \pm 5\%$  (weighted mean  $\pm$  standard error), as observed in four out of five subjects except subject 1.

#### 4.4 Subject-by-subject Alignment

Figure 5b displays the confusion matrices of subject-by-subject alignment for four  $n$ -back tasks (0, 1, 2, and 3) of five subjects. We used the barycenter and its corresponding labels calculated from FG-W as a new representation of the labeled fNIRS data from all four sessions of one subject (the source subject), and then aligned that barycenter to unlabeled data from each session of other subject (the target subject). Each number in the reported confusion matrix is the average of alignment accuracy of different tasks from the source subject to four other subjects as the targets. Details of subject-by-subject alignment from barycenter of source subject to four sessions of the target subject are shown in Appendix, Table 3. Average subject-by-subject alignment accuracy is shown in Table 1. Each reported accuracy value in Table 1 is the average of the alignment accuracy when considering one subject as the source and four other subjects as the targets. For the  $n$ -back task classification with CNN, data from all four sessions from one subject were used as input and

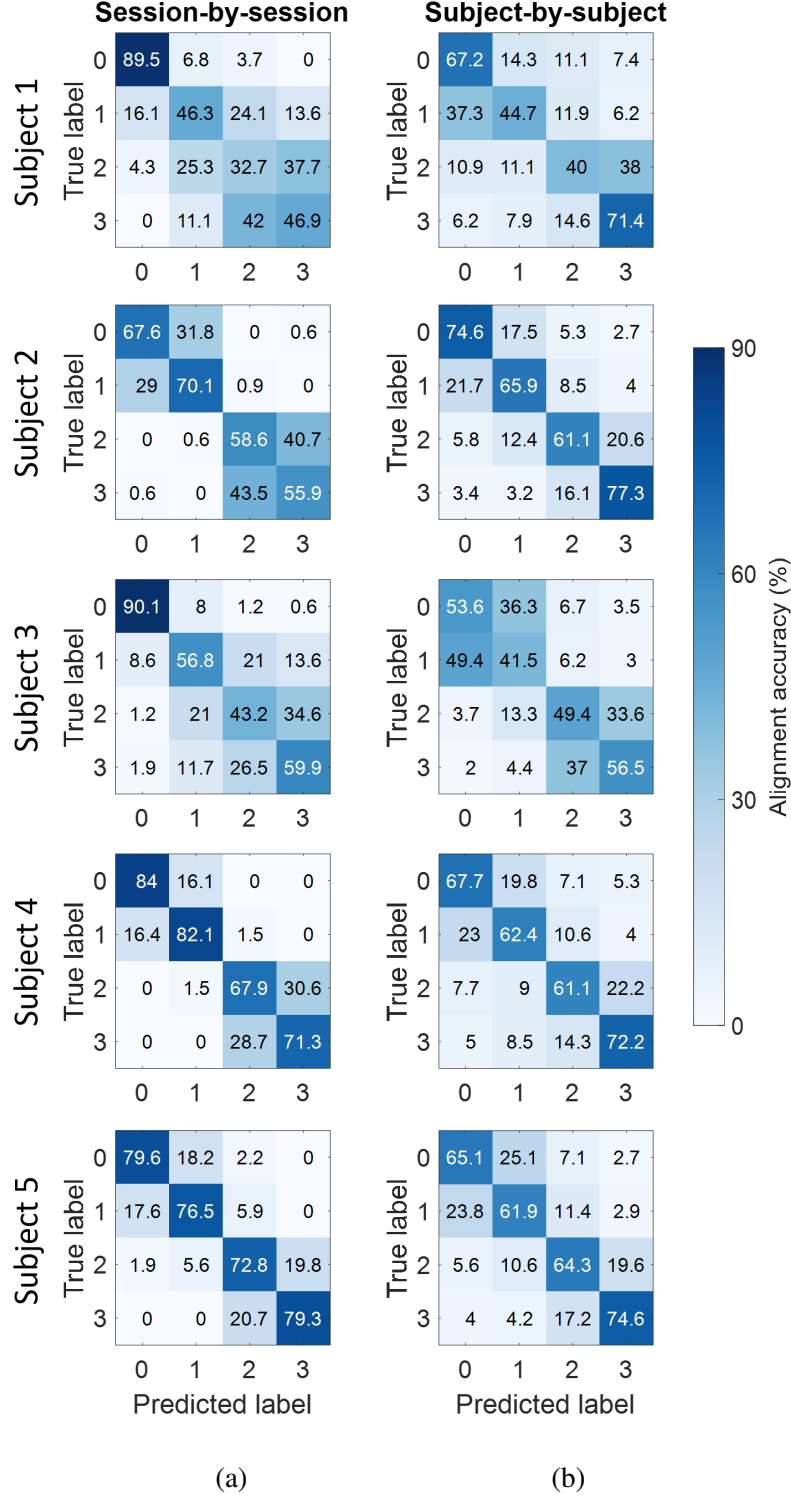


Fig 5: Confusion matrices of session-by-session and subject-by-subject alignments in five subjects. The first column (a) presents session-by-session alignment accuracy within each subject. Each number reported in each confusion matrix is the average accuracy from the alignment of every two separate sessions among four sessions. The second column (b) presents subject-by-subject alignment accuracy. Each number reported is the average accuracy from the alignment between one source subject to other four target subjects.

the classification model was trained to predict the task labels for all other four subjects in the same manner as in Section 4.3. We can see that FG-W barycenter algorithm still works well even with large domain shift and outperforms its counterpart. Compared to CNN, our method achieved a higher alignment accuracy by an average of  $6 \pm 2\%$  (weighted mean  $\pm$  standard error), as observed in all subjects.

Since subject 3 has poor SNR and severe motion artifacts in half of the fNIRS data which were discarded during the pre-processing step, we treat this subject as an outlier and report the alignment accuracy without subject 3 in Table 4 and Table 5 in Appendix.

#### 4.5 Combining $n$ -back tasks in Session-by-session and Subject-by-subject Alignment

The analysis of subject performance (Section 4.1) showed significant differences in the number of missed targets and wrong reactions depending on the  $n$ -back task conditions. Particularly, subject performance suggests that 0- and 1-back tasks could be combined together in the alignment since they show similar brain activation behaviors. In this section, we showed that by combining data from 0-back together with 1-back, and 2-back together with 3-back tasks, the alignment accuracy increased abruptly for both session-by-session and subject-by-subject alignment, as shown in Table 2. As compared to results reported in Table 1, session-by-session alignment accuracy increased by an average of  $22 \pm 2\%$  (weighted mean  $\pm$  standard error), and subject-by-subject alignment accuracy increased by an average of  $34 \pm 3\%$ .

Table 2: Average session-by-session and subject-by-subject alignment accuracy (%) from G-W and FG-W methods, respectively, when combining 0-back together with 1-back tasks, and 2-back together with 3-back tasks. Cleaned fNIRS data were used.

|                    | Subject 1   | Subject 2  | Subject 3   | Subject 4   | Subject 5  |
|--------------------|-------------|------------|-------------|-------------|------------|
| Session-by-session | $79 \pm 8$  | $99 \pm 2$ | $82 \pm 17$ | $99 \pm 1$  | $96 \pm 2$ |
| Subject-by-subject | $82 \pm 12$ | $89 \pm 9$ | $89 \pm 3$  | $86 \pm 14$ | $88 \pm 7$ |

## 5 Discussion

In this study of five subjects, we show that fNIRS signals measured from 20 channels on the PFC can be used to robustly discriminate subjects' mental workload between different  $n$ -back task levels across sessions within one subject and across different subjects. We thereby showed the potential of fNIRS as a modality for BCI and user state monitoring that can adapt to different users with various physiological states.

In regards to data pre-processing, we show that motion artifact removal in fNIRS signals is an important step for the following mental workload alignment. Specifically, we report that using TARA to remove motion artifacts from fNIRS signals increased alignment accuracy by an average of  $13 \pm 3\%$  for session-by-session alignment and by  $11 \pm 2\%$  for subject-by-subject alignment. Future work could include addressing different types of artifacts that could arise in fNIRS time series which were not considered by TARA, such as oscillatory transients. Additionally, possible future improvements in TARA may be to investigate an automatic way for selection of regularization and non-convexity parameters in TARA algorithm across subjects.

Based on the multiple sessions and subjects data obtained from the experiment, we introduced two approaches, G-W and FG-W barycenter, for session-by-session and subject-by-subject alignment of mental workload during  $n$ -back task. We revealed that our methods could be generalized across different sessions and subjects data with a limited amount of labeled data. Specifically, for session-by-session alignment, we only needed labeled fNIRS data acquired during some known  $n$ -back task conditions from one session of one subject to align with other unlabeled sessions from the same subject. Using G-W matching method, we showed that most of the labels could be mapped correctly to the other sessions' data within the same subject, with the alignment accuracy

ranging from 54 to 77% (with 25% representing chance alignment). Meanwhile, with the same amount of data from one session for training using CNN, the  $n$ -back task classification accuracy was poorly achieved (by an average of  $7 \pm 5\%$  less than G-W in performance accuracy, reported as weighted mean  $\pm$  standard error). Similarly for subject-by-subject alignment, we only needed labeled data from one subject as the source data for alignment. Labels and structural information of the source data were combined to generate a new representation (i.e. the FG-W barycenter). Following the same routine as the session-by-session alignment, we were able to use the barycenter from the source subject to predict the labels for data from different sessions for other subjects, with the alignment accuracy ranging from 51 to 68% (also with 25% representing chance alignment). Again, when data from one subject were used to train CNN,  $n$ -back task classification performance achieved lower accuracy than our method (by an average of  $6 \pm 2\%$  less than FG-W in performance accuracy). Moreover, for CNN method, we needed to interpolate the data such that all the data has the same dimension (e.g., in the case of subject 3), which isn't regarded as a requirement in our method. However, we also found that although our method is free from the dimension requirement for data, when a large amount of data is missing (e.g., in the case of subject 3 when around half of the channels were discarded in the pre-processing step), our method still couldn't achieve a satisfying result.

From the alignment results, we found relatively higher alignment results for session-by-session alignment ( $70 \pm 4\%$ ) than subject-by-subject alignment ( $55 \pm 3\%$ ). In fact, this behavior is observed significantly in three out of five subjects (subjects 3, 4 and 5), and the alignment accuracy was relatively similar in the remaining subjects (subjects 1 and 2). This is reasonable since we expect the data variations across subjects to be larger than the variations across sessions for one subject. However, we found that even though subject-by-subject alignment was a more challenging

problem due to the higher variations across subjects, the new representation of the barycenter of the source subject aligned well to data from other subjects, which indicates that different subjects may still share similar underlying structures even from different domains. Future work will explore generating barycenter from source data from multiple subjects' information for subject-by-subject alignment.

Based on our alignment results shown in confusion matrices in Fig. 5, the misalignment in session-by-session and subject-by-subject alignment are relatively high between 0-back and 1-back, and between 2-back and 3-back tasks. In particular, the misalignment is the highest between 2- and 3-back task (when 2-back task is the true label and 3-back is the predicted label and vice versa), ranging from 19.8 to 43.5%. The second highest misalignment is between 0- and 1-back task, ranging from 6.8 to 31.8%. Similarly, for subject-by-subject alignment, the highest misalignment came from 0- and 1-back task, ranging from 14.3 to 49.4%. The second highest misalignment is between 2- and 3-back, ranging from 14.3 to 38%. This gave us an idea of combining 0- with 1-back tasks, and 2- with 3-back tasks in the alignment. Substantial increases in alignment performance (by an average of 22% for session-by-session and 34% for subject-by-subject alignment) suggest that future studies could investigate the workload classification between rest to low workload level (0- and 1-back tasks) versus high workload level (2- and 3-back tasks).

Finally, in this work we reported alignment accuracy from single-distance continuous-wave fNIRS measurements of intensity from source-detector pairs at 3 cm distance. This measurements are sensitive to hemodynamic changes both in superficial tissues (i.e., scalp and skull) and in the brain.<sup>59</sup> For the purpose of our aims, it is desirable to increase the sensitivity of our measurements to brain tissue, in order to probe hemodynamic changes associated with brain activation. One approach, namely the dual-slope method, involves a simple implementation of a certain arrangement



of sources and detectors to localize sensitivity of NIRS measurements to a deeper region,<sup>60</sup> thus suppressing confounding signals from superficial tissue. This approach could also help remove instrumental drifts and motion artifacts from measured signals as dual-slopes are unaffected by changes in optical coupling. Future extensions of this work may involve implementing the dual-slope configuration in such experiments as those described here.

## 6 Appendix

Table 3: Subject-by-subject alignment accuracy (%). The left arrow means the alignment is from the barycenter of the source subject in left (the 1<sup>st</sup> subject) to data in each of the four sessions of the target subject in the right (the 2<sup>nd</sup> subject) and vice versa. '-' means the session of the subject is discarded due to its high level of noise.

| Session | Subject alignment (1 <sup>st</sup> subject - 2 <sup>nd</sup> subject) |    |     |    |     |    |     |    |     |    |     |    |     |    |     |    |     |    |     |    |
|---------|---|----|-----|----|-----|----|-----|----|-----|----|-----|----|-----|----|-----|----|-----|----|-----|----|
|         | 1-2   |    | 1-3 |    | 1-4 |    | 1-5 |    | 2-3 |    | 2-4 |    | 2-5 |    | 3-4 |    | 3-5 |    | 4-5 |    |
|         | →   | ←  | →   | ←  | →   | ←  | →   | ←  | →   | ←  | →   | ←  | →   | ←  | →   | ←  | →   | ←  | →   | ←  |
| 1       | 60  | 64 | 15  | 48 | 69  | 62 | 56  | 55 | 36  | 32 | 88  | 77 | 69  | 70 | 58  | 12 | 44  | 69 | 77  | 80 |
| 2       | 55  | 69 | 53  | 54 | 63  | 64 | 70  | 54 | 69  | 55 | 81  | 92 | 84  | 73 | 47  | 72 | 56  | 67 | 85  | 69 |
| 3       | 60  | 60 | 32  | 50 | 73  | 64 | 71  | 67 | 29  | 63 | 81  | 69 | 83  | 79 | 55  | 28 | 61  | 33 | 60  | 84 |
| 4       | 56  | -  | -   | -  | 43  | -  | 61  | -  | -   | 35 | 89  | 86 | 74  | 66 | 31  | -  | 65  | -  | 75  | 70 |
| Avg     | 58  | 64 | 33  | 51 | 62  | 63 | 65  | 59 | 45  | 46 | 85  | 81 | 78  | 72 | 48  | 37 | 57  | 56 | 74  | 76 |

Table 4: Subject-by-subject alignment accuracy without subject 3 (%).

| Session | Subject alignment (1 <sup>st</sup> subject - 2 <sup>nd</sup> subject) |    |     |    |     |    |     |    |     |    |     |    |
|---------|---|----|-----|----|-----|----|-----|----|-----|----|-----|----|
|         | 1-2   |    | 1-4 |    | 1-5 |    | 2-4 |    | 2-5 |    | 4-5 |    |
|         | →   | ←  | →   | ←  | →   | ←  | →   | ←  | →   | ←  | →   | ←  |
| 1       | 60  | 64 | 69  | 62 | 56  | 55 | 88  | 77 | 69  | 70 | 77  | 80 |
| 2       | 55  | 69 | 63  | 64 | 70  | 54 | 81  | 92 | 84  | 73 | 85  | 69 |
| 3       | 60  | 60 | 73  | 64 | 71  | 67 | 81  | 69 | 83  | 79 | 60  | 84 |
| 4       | 56  | -  | 43  | -  | 61  | -  | 89  | 86 | 74  | 66 | 75  | 70 |
| Avg     | 58  | 64 | 62  | 63 | 65  | 59 | 85  | 81 | 78  | 72 | 74  | 76 |

Table 5: Average subject-by-subject alignment accuracy (%) without subject 3. Reported values are obtained from Table 4 as the averages of all the alignment accuracy when considering one subject as the source and other four subjects as the target.

|             | Subject 1 | Subject 2 | Subject 4 | Subject 5 |
|-------------|-----------|-----------|-----------|-----------|
| G-W cleaned | 62 ± 3    | 76 ± 9    | 73 ± 7    | 69 ± 7    |

Table 6: CNN architecture, where  $d$  = number of channels (40 in our case),  $w$  = number of time points (60 in our case),  $T_1, T_2$  = length of time points after applying the filter and  $C$  = number of classes (4 in our case).

| Layer           | Operation  | Output Size    |
|-----------------|--|----------------|
| Input           | –  | $(2, d, w)$    |
| Conv2D          | 20 * filter (1, 10)+BatchNorm+ReLU+Dropout(0.2)    | $(20, d, T_1)$ |
| Conv2D          | 20 * filter (1, 5)+BatchNorm+ReLU+Dropout(0.2)     | $(20, d, T_2)$ |
| DepthwiseConv2D | 20 * kernel ( $d, 1$ )+BatchNorm+ReLU+Dropout(0.2) | $(20, 1, T_2)$ |
| –               | Flatten  | $(20 * T_2)$   |
| Dense *2        | –  | $C$            |

### *Disclosures*

The authors have no relevant financial interests in this manuscript and no potential conflicts of interest to disclose.

### *Acknowledgments*

We thank Angelo Sassaroli for useful discussions. This material is based upon work supported by the Air Force Office of Scientific Research under award number FA9550-18-1-0465. Any opinions, finding, and conclusions or recommendations expressed in this material are those of the author(s) and do not necessarily reflect the view of the United States Air Force. Shuchin Aeron would like to acknowledge support by NSF CAREER award CCF:1553075.

### *Code, Data, and Materials Availability*

The code used to generate the results and figures is available in the Github repository:

[https://github.com/boyanglyu/nback\\_align](https://github.com/boyanglyu/nback_align).

## References

- 1 M. A. Franceschini, V. Toronov, M. E. Filiaci, *et al.*, “On-line optical imaging of the human brain with 160-ms temporal resolution,” *Optics Express* **6**, 49–57 (2000).
- 2 M. Wolf, U. Wolf, V. Toronov, *et al.*, “Different Time Evolution of Oxyhemoglobin and Deoxyhemoglobin Concentration Changes in the Visual and Motor Cortices during Functional Stimulation: A Near-Infrared Spectroscopy Study,” *NeuroImage* **16**(3), 704—712 (2002).
- 3 D. A. Boas, T. Gaudette, G. Strangman, *et al.*, “The Accuracy of Near Infrared Spectroscopy and Imaging during Focal Changes in Cerebral Hemodynamics,” *NeuroImage* **13**(1), 76–90 (2001).
- 4 K. Bejm, S. Wojtkiewicz, P. Sawosz, *et al.*, “Influence of contrast-reversing frequency on the amplitude and spatial distribution of visual cortex hemodynamic responses,” *Biomedical Optics Express* **10**(12), 6296 (2019).
- 5 M. J. Herrmann, M. M. Plichta, A.-C. Ehlis, *et al.*, “Optical topography during a Go–NoGo task assessed with multi-channel near-infrared spectroscopy,” *Behavioural Brain Research* **160**(1), 135–140 (2005).
- 6 X. Cui, D. M. Bryant, and A. L. Reiss, “NIRS-Based Hyperscanning Reveals Increased Interpersonal Coherence in Superior Frontal Cortex during Cooperation,” *NeuroImage* **59**(3), 2430–2437 (2012).
- 7 P. Pinti, I. Tachtsidis, A. Hamilton, *et al.*, “The present and future use of functional near-infrared spectroscopy (fNIRS) for cognitive neuroscience,” *Annals of the New York Academy of Sciences* **1464**(1), 5–29 (2020).
- 8 S. Coyle, T. Ward, C. Markham, *et al.*, “On the suitability of near-infrared (NIR) systems

- for next-generation brain–computer interfaces,” *Physiological Measurement* **25**(4), 815–822 (2004).
- 9 A. Bosworth, M. Russell, and R. J. K. Jacob, “Update of fNIRS as an Input to Brain–Computer Interfaces: A Review of Research from the Tufts Human–Computer Interaction Laboratory,” *Photonics* **6**(3), 90 (2019).
  - 10 K.-S. Hong, U. Ghafoor, and M. J. Khan, “Brain–machine interfaces using functional near-infrared spectroscopy: a review,” *Artificial Life and Robotics* **25**, 204—218 (2020).
  - 11 A. M. Owen, K. M. Mcmillan, A. R. Laird, *et al.*, “N-back working memory paradigm: A meta-analysis of normative functional neuroimaging studies,” *Human Brain Mapping* **25**(1), 46–59 (2005).
  - 12 E. E. Smith and J. Jonides, “Working Memory: A View from Neuroimaging,” *Cognitive Psychology* **33**(1), 5–42 (1997).
  - 13 J. Shin, A. V. Lüthmann, D.-W. Kim, *et al.*, “Simultaneous acquisition of EEG and NIRS during cognitive tasks for an open access dataset,” *Scientific Data* **5**(1) (2018).
  - 14 C. Herff, D. Heger, O. Fortmann, *et al.*, “Mental workload during n-back task—quantified in the prefrontal cortex using fNIRS,” *Frontiers in Human Neuroscience* **7** (2014).
  - 15 Y. Hoshi, B. Tsou, V. Billock, *et al.*, “Spatiotemporal Characteristics of Hemodynamic Changes in the Human Lateral Prefrontal Cortex During Working Memory Tasks,” *NeuroImage* **20**(3), 1493–1504 (2004).
  - 16 H. Aghajani, M. Garbey, and A. Omurtag, “Measuring Mental Workload with EEG+fNIRS,” *Front. Hum. Neurosci.* **11**, 359 (2017).

- 17 E. B. Coffey, A.-M. Brouwer, and J. B. van Erp, “Measuring workload using a combination of electroencephalography and near infrared spectroscopy,” *Proceedings of the Human Factors and Ergonomics Society Annual Meeting* **56**(1), 1822—1826 (2012).
- 18 T. Nakano, H. Watanabe, F. Homae, *et al.*, “Prefrontal Cortical Involvement in Young Infants Analysis of Novelty,” *Cerebral Cortex* **19**, 455–463 (2008).
- 19 M. R. Siddiquee, J. S. Marquez, R. Atri, *et al.*, “Movement artefact removal from NIRS signal using multi-channel IMU data,” *BioMedical Engineering OnLine* **17**(1), 120 (2018).
- 20 Q. Zhang, G. E. Strangman, and G. Ganis, “Adaptive filtering to reduce global interference in non-invasive NIRS measures of brain activation: How well and when does it work?,” *NeuroImage* **45**(3), 788–794 (2009).
- 21 J. Gervain, F. Macagno, S. Cogoi, *et al.*, “The neonate brain detects speech structure,” *Proceedings of the National Academy of Sciences* **105**(37), 14222–14227 (2008).
- 22 M. Pena, A. Maki, D. Kovacic, *et al.*, “Sounds and silence: An optical topography study of language recognition at birth,” *Proceedings of the National Academy of Sciences* **100**(20), 11702–11705 (2003).
- 23 F. Scholkmann, S. Spichtig, T. Muehlmann, *et al.*, “How to detect and reduce movement artifacts in near-infrared imaging using moving standard deviation and spline interpolation,” *Physiological Measurement* **31**(5), 649–662 (2010).
- 24 X. Cui, S. Bray, and A. L. Reiss, “Functional near infrared spectroscopy (NIRS) signal improvement based on negative correlation between oxygenated and deoxygenated hemoglobin dynamics,” *NeuroImage* **49**(4), 3039–3046 (2010).

- 25 M. Izzetoglu, P. Chitrapu, S. Bunce, *et al.*, “Motion artifact cancellation in NIR spectroscopy using discrete Kalman filtering,” *BioMedical Engineering OnLine* **9**(1), 16 (2010).
- 26 A. V. Medvedev, J. Kainerstorfer, S. V. Borisov, *et al.*, “Event-related fast optical signal in a rapid object recognition task: Improving detection by the independent component analysis,” *Brain Research* **1236**, 145–158 (2008).
- 27 F. C. Robertson, T. S. Douglas, and E. M. Meintjes, “Motion Artifact Removal for Functional Near Infrared Spectroscopy: A Comparison of Methods,” *IEEE Transactions on Biomedical Engineering* **57**(6), 1377–1387 (2010).
- 28 H. Sato, N. Tanaka, M. Uchida, *et al.*, “Wavelet analysis for detecting body-movement artifacts in optical topography signals,” *NeuroImage* **33**(2), 580–587 (2006).
- 29 I. W. Selesnick, H. L. Graber, Y. Ding, *et al.*, “Transient Artifact Reduction Algorithm (TARA) Based on Sparse Optimization,” *IEEE Transactions on Signal Processing* **62**(24), 6596–6611 (2014).
- 30 S. Ben-David, J. Blitzer, K. Crammer, *et al.*, “A theory of learning from different domains,” *Machine learning* **79**(1-2), 151–175 (2010).
- 31 W. M. Kouw and M. Loog, “A review of domain adaptation without target labels,” *IEEE Transactions on Pattern Analysis and Machine Intelligence* , 1–1 (2019).
- 32 V. K. Kurmi and V. P. Namboodiri, “Looking back at labels: A class based domain adaptation technique,” in *2019 International Joint Conference on Neural Networks (IJCNN)*, 1–8, IEEE (2019).
- 33 H. Shimodaira, “Improving predictive inference under covariate shift by weighting the log-likelihood function,” *Journal of statistical planning and inference* **90**(2), 227–244 (2000).

- 34 G. Peyré and M. Cuturi, “Computational Optimal Transport: With Applications to Data Science,” *Foundations and Trends® in Machine Learning* **11**(5-6), 355–607 (2019).
- 35 J. Solomon, G. Peyré, V. G. Kim, *et al.*, “Entropic metric alignment for correspondence problems,” *ACM Transactions on Graphics (TOG)* **35**(4), 1–13 (2016).
- 36 F. Mémoli, “Gromov–Wasserstein distances and the metric approach to object matching,” *Foundations of computational mathematics* **11**(4), 417–487 (2011).
- 37 N. Courty, R. Flamary, D. Tuia, *et al.*, “Optimal transport for domain adaptation,” *IEEE transactions on pattern analysis and machine intelligence* **39**(9), 1853–1865 (2016).
- 38 O. Yair, F. Dietrich, R. Talmon, *et al.*, “Optimal transport on the manifold of SPD matrices for domain adaptation,” *arXiv preprint arXiv:1906.00616* (2019).
- 39 N. T. Gayraud, A. Rakotomamonjy, and M. Clerc, “Optimal transport applied to transfer learning for p300 detection,” (2017).
- 40 G. Peyré, M. Cuturi, and J. Solomon, “Gromov-Wasserstein Averaging of Kernel and Distance Matrices,” in *Proceedings of The 33rd International Conference on Machine Learning, Proceedings of Machine Learning Research* **48**, 2664–2672, PMLR, (New York, New York, USA) (2016).
- 41 V. Titouan, N. Courty, R. Tavenard, *et al.*, “Optimal transport for structured data with application on graphs,” in *International Conference on Machine Learning*, 6275–6284 (2019).
- 42 V. Jurcak, D. Tsuzuki, and I. Dan, “10/20, 10/10, and 10/5 systems revisited: Their validity as relative head-surface-based positioning systems,” *NeuroImage* **34**(4), 1600–1611 (2007).
- 43 A. Sassaroli and S. Fantini, “Comment on the modified Beer-Lambert law for scattering media,” *Physics in Medicine & Biology* **49**(14), N255—N257 (2004).

- 44 I. J. Bigio and S. Fantini, *Quantitative Biomedical Optics: Theory, Methods, and Applications*, Cambridge University Press, USA, 1st ed. (2016).
- 45 L. Kantorovich, “On the transfer of masses (in russian),” in *Doklady Akademii Nauk*, **37**(2), 227–229 (1942).
- 46 G. Monge, “Mémoire sur la théorie des déblais et des remblais,” *Histoire de l’Académie Royale des Sciences de Paris* (1781).
- 47 M. Cuturi, “Sinkhorn distances: Lightspeed computation of optimal transport,” in *Advances in neural information processing systems*, 2292–2300 (2013).
- 48 R. Sinkhorn, “Diagonal equivalence to matrices with prescribed row and column sums. II,” *Proceedings of the American Mathematical Society* **45**(2), 195–198 (1974).
- 49 B. K. Abid and R. M. Gower, “Greedy stochastic algorithms for entropy-regularized optimal transport problems,” *arXiv preprint arXiv:1803.01347* (2018).
- 50 J. Altschuler, J. Niles-Weed, and P. Rigollet, “Near-linear time approximation algorithms for optimal transport via Sinkhorn iteration,” in *Advances in Neural Information Processing Systems*, 1964–1974 (2017).
- 51 A. Barachant, S. Bonnet, M. Congedo, *et al.*, “Classification of covariance matrices using a Riemannian-based kernel for BCI applications,” *Neurocomputing* **112**, 172–178 (2013).
- 52 D. Heger, R. Mutter, C. Herff, *et al.*, “Continuous Recognition of Affective States by Functional Near Infrared Spectroscopy Signals,” in *2013 Humaine Association Conference on Affective Computing and Intelligent Interaction*, 832–837 (2013).
- 53 R. Bhatia, S. Gaubert, and T. Jain, “Matrix versions of the Hellinger distance,” *Letters in Mathematical Physics* **109**(8), 1777–1804 (2019).



- 54 T. Vayer, L. Chapel, R. Flamary, *et al.*, “Fused Gromov-Wasserstein distance for structured objects: theoretical foundations and mathematical properties,” (2018).
- 55 A. Barachant, S. Bonnet, M. Congedo, *et al.*, “Multiclass Brain–Computer Interface Classification by Riemannian Geometry,” *IEEE Transactions on Biomedical Engineering* **59**(4), 920–928 (2012).
- 56 L. McInnes, J. Healy, and J. Melville, “UMAP: Uniform manifold approximation and projection for dimension reduction,” *arXiv preprint arXiv:1802.03426* (2018).
- 57 V. J. Lawhern, A. J. Solon, N. R. Waytowich, *et al.*, “EEGNet: a compact convolutional neural network for EEG-based brain–computer interfaces,” *Journal of Neural Engineering* **15**, 056013 (2018).
- 58 D. P. Kingma and J. Ba, “Adam: A Method for Stochastic Optimization,” (2014).
- 59 I. Tachtsidis and F. Scholkmann, “False positives and false negatives in functional near-infrared spectroscopy: Issues, challenges, and the way forward,” *Neurophotonics* **3**(3), 031405 (2016).
- 60 A. Sassaroli, G. Blaney, and S. Fantini, “Dual-slope method for enhanced depth sensitivity in diffuse optical spectroscopy,” *J. Opt. Soc. Am. A* **36**(10), 1743–1761 (2019).

**Boyang Lyu** is a Ph.D. student at Tufts University under Prof. Shuchin Aeron. Her research involves unsupervised domain adaptation and signal processing. She has applied some of these techniques to word alignment and mental workload identification.

**Thao Pham** is a Ph.D. student in the Diffuse Optical Imaging of Tissue (DOIT) Lab at Tufts University, under Prof. Sergio Fantini. Her research interests involve using near-infrared spec-

troscopy (NIRS) and coherent hemodynamics spectroscopy (CHS) model for noninvasive monitoring of cerebral blood flow (CBF) and cerebral hemodynamics in healthy human subjects and in clinical settings.

**Giles Blaney** is a Ph.D. student in the Diffuse Optical Imaging of Tissue (DOIT) lab at Tufts University under Prof. Sergio Fantini. He received a Bachelor of Science in Mechanical Engineering and Physics from Northeastern University in 2017, with minors in Electrical Engineering and Mathematics. Currently, Giles is researching methods for depth discrimination and imaging for use in near-infrared spectroscopy (NIRS). This includes studying the sensitivity of various NIRS optode arrangements in heterogeneous media, and development of the dual-slope method.

**Sergio Fantini** is Professor of Biomedical Engineering and principal investigator of the “Diffuse Optical Imaging of Tissue Laboratory” (DOIT Lab) at Tufts University. The DOIT Lab aims to develop non-invasive applications of near-infrared spectroscopy for medical diagnostics, monitoring of tissue oxygenation, quantitative assessment of tissue perfusion, and functional imaging. He co-authored with Dr. Irving Bigio a textbook on “Quantitative Biomedical Optics” published by Cambridge University Press. He is a Fellow of OSA, SPIE, and AIMBE.

**Shuchin Aeron** is an Associate Professor in the Dept. of ECE at Tufts University. Prior to Tufts he was a post-doctoral research scientist at Schlumberger Doll Research, Cambridge, MA from 2009-2011. He was awarded the School Of Engineering and Electrical and Computer Engineering Best Thesis Award. He is a recipient of the NSF CAREER award (2016). His main research interest lies at the intersection of information theory, statistical signal processing, optimization, and machine learning.

Biographies and photographs of the other authors are not available.

## List of Figures

- 1 (a) Experimental design for  $n$ -back task. (b) fNIRS headset with eight sources and seven detectors to give a total of 20 channels at source-detector distance of 3 cm. (c) A zoomed-in view of the schematic in (b) showing the 10-10 and 10-5 system positions covered by the sources and detectors.
- 2 Summary of subject performance for the  $n$ -back task: average percentages of wrong responses (a) and missed responses (b) for  $n$ -back task conditions across subjects. Bars represent the mean, and error bars represent standard errors across four experimental sessions.
- 3 The top row shows the original and cleaned signal. The second row shows the detected motion artifacts, including spike- and step-like features. The cleaned signal is obtained by subtracting these motion artifact features from the original signal. The last row shows the low-pass filtered signal of the original data. Distortion in the signal arisen from the step discontinuity can still be observed from the low-pass filtered signal.
- 4 Visualization of the alignment from session 1 to session 2 for subject 4. Circles indicate data from session 1 and triangles indicate the data from session 2. Four different colors represent 0- to 3-back experiments. Black lines indicate correct alignment and red lines indicate misalignment.

- 5 Confusion matrices of session-by-session and subject-by-subject alignments in five subjects. The first column (a) presents session-by-session alignment accuracy within each subject. Each number reported in each confusion matrix is the average accuracy from the alignment of every two separate sessions among four sessions. The second column (b) presents subject-by-subject alignment accuracy. Each number reported is the average accuracy from the alignment between one source subject to other four target subjects.

## List of Tables

- 1 Average session-by-session and subject-by-subject alignment accuracy (%) by using G-W and FG-W, respectively, as compared with CNN. G-W and FG-W barycenter alignment methods are applied to both original data and data cleaned by TARA algorithm. For CNN, only cleaned data are used as input.
- 2 Average session-by-session and subject-by-subject alignment accuracy (%) from G-W and FG-W methods, respectively, when combining 0-back together with 1-back tasks, and 2-back together with 3-back tasks. Cleaned fNIRS data were used.
- 3 Subject-by-subject alignment accuracy (%). The left arrow means the alignment is from the barycenter of the source subject in left (the 1<sup>st</sup> subject) to data in each of the four sessions of the target subject in the right (the 2<sup>nd</sup> subject) and vice versa. '-' means the session of the subject is discarded due to its high level of noise.
- 4 Subject-by-subject alignment accuracy without subject 3 (%).

- 5 Average subject-by-subject alignment accuracy (%) without subject 3. Reported values are obtained from Table 4 as the averages of all the alignment accuracy when considering one subject as the source and other four subjects as the target.
- 6 CNN architecture, where  $d$  = number of channels (40 in our case),  $w$  = number of time points (60 in our case),  $T_1, T_2$  = length of time points after applying the filter and  $C$  = number of classes (4 in our case).